How grow-and-switch gravitropism generates root coiling and root waving growth responses in *Medicago truncatula*

Tzer Han Tan[a,1], Jesse L. Silverberg[b], Daniela S. Floss[c], Maria J. Harrison[c], Christopher L. Henley[b,2], and Itai Cohen[b]

[a]Department of Applied and Engineering Physics, Cornell University, Ithaca, NY 14853; [b]Department of Physics, Cornell University, Ithaca, NY 14853; and [c]Boyce Thompson Institute for Plant Research, Cornell University, Ithaca, NY 14853

Edited by William Bialek, Princeton University, Princeton, NJ, and approved September 1, 2015 (received for review May 21, 2015)

Experimental studies show that plant root morphologies can vary widely from straight gravity-aligned primary roots to fractal-like root architectures. However, the opaqueness of soil makes it difficult to observe how environmental factors modulate these patterns. Here, we combine a transparent hydrogel growth medium with a custom built 3D laser scanner to directly image the morphology of *Medicago truncatula* primary roots. In our experiments, root growth is obstructed by an inclined plane in the growth medium. As the tilt of this rigid barrier is varied, we find *Medicago* transitions between randomly directed root coiling, sinusoidal root waving, and normal gravity-aligned morphologies. Although these root phenotypes appear morphologically distinct, our analysis demonstrates the divisions are less well defined, and instead, can be viewed as a 2D biased random walk that seeks the path of steepest decent along the inclined plane. Features of this growth response are remarkably similar to the widely known run-and-tumble chemotactic behavior of *Escherichia coli* bacteria, where biased random walks are used as optimal strategies for nutrient uptake.

plant biomechanics | root morphology | root waving | root coiling | pattern formation

Plants are able to sense a wide variety of external stimuli, giving rise to actively controlled responses driven by gradients in light, gravity, touch, nutrient resources, and water. These responses, which include phototropism, gravitropism, thigmotropism, chemotropism, and hydrotropism, take input from the local environment and modulate phenotype development in a manner essential for survival (1–5). A number of plant growth responses, such as the popping of chiral seed pods (6) and the overwinded morphology of cucumber tendrils (7), are dominated by the mechanical properties of plant tissues and their passive response to physical forces. However, these special cases aside, growth patterns are more typically modulated by a combination of actively regulated biological processes and passive mechanical response. The snapping of a Venus fly trap (8–11) is a classic example, where cell turgor pressure and thin shell mechanics work in tandem to determine the plant's phenotype. Continued studies of developmental morphology at the interface between mechanical and biological regulation play an essential role in bridging phenotypic and biomolecular points of view (12, 13), while offering a more complete understanding of plant biomechanics.

In the context of roots, the mechanical properties of the growth medium play a critical role in modulating root morphology, as evidenced by a variety of studies examining the role of soil impedance (14–19), granularity (20), the presence of cracks (21), and mechanical barriers (22–24). For example, experiments with *Arabidopsis thaliana* primary roots show that normal gravity-aligned morphologies interrupted by a horizontal barrier lead to an in-plane coiling of the root. As the barrier is tilted, a combination of active and passive growth responses drive root waving (25–30). In these conditions, the primary root exhibits sinusoidal growth that deviates from a strict downward direction along the plane. Early experimental work accounted for the waving morphology as a combination of positive gravitropism and a thigmotropic (growth response to touch) effect (25). This interpretation relied on the barrier to simultaneously prevent gravity-aligned growth and activate a thigmotropic twisting of the root tip; however, later experiments demonstrated a role for friction as an additional contributing factor (28). Although *Arabidopsis* mutants have been used to explore the underlying genetic regulatory pathways of root waving, the detailed mechanism coupling gravity sensing and the growth environment's mechanical properties is still open to debate (27, 29, 30).

While these initial studies have proposed different mechanisms for root waving, it remains unknown whether the phenomenon is species-specific or a generic root growth strategy. Here, we perform experiments on *Medicago truncatula*, a model legume, and find growth patterns similar to root waving. This plant is larger than *Arabidopsis* and fast-growing, which makes it convenient for study. Our experiments combine 3D imaging with a controlled mechanical growth environment that interpolates between a horizontal physical barrier and normal unobstructed growth. This approach allows us to nondestructively examine the in situ root development and quantify the resulting morphology with a variety of geometric and statistical metrics. Whereas previous studies have focused on temporal dynamics and genetic components of root waving, we turn our attention to the growth barrier's tilt angle and subsequently probe different aspects of the phenomenon. Ultimately, our analysis reveals a mechanism that produces root waving as a byproduct of gravitropic reorientation on the mechanical barrier, and the root's measurement tolerance for the direction of gravity.

Experimental Procedures

Medicago seedlings were germinated and transferred to transparent chambers containing growth media with Gelrite, which provided both moderate mechanical impedance to root growth and an abundant source of nutrients (see *SI Appendix, SI Materials and Methods*; also see ref. 31). In

Significance

Root waving, a growth response previously discussed predominantly in *Arabidopsis*, is reported in *Medicago truncatula*. Analogous to bacterial chemotaxis where *Escherichia coli* uses a "run-and-tumble" strategy to find sources of food, our experiments reveal a "grow-and-switch" gravitropic response in these root systems. This finding offers valuable insights into the strategies used for plants as they navigate heterogeneous environments in search of water and nutrient resources.

Author contributions: T.H.T., J.L.S., D.S.F., M.J.H., C.L.H., and I.C. designed research; T.H.T. and D.S.F. performed research; T.H.T. contributed new reagents/analytic tools; T.H.T., J.L.S., C.L.H., and I.C. analyzed data; and T.H.T., J.L.S., D.S.F., M.J.H., C.L.H., and I.C. wrote the paper.

The authors declare no conflict of interest.

This article is a PNAS Direct Submission.

[1]To whom correspondence should be addressed. Email: tzerhan@mit.edu.

[2]Deceased June 29, 2015.

This article contains supporting information online at www.pnas.org/lookup/suppl/doi:10.1073/pnas.1509942112/-/DCSupplemental.

total, 92 plants were germinated, with each growth chamber containing one plant; 87 samples were analyzed in this work, whereas the remaining 5 exhibited atypical stunted growth and were excluded from our analysis. To systematically study root waving, we introduced a physical barrier in the growth medium tilted at an angle θ, measured from the horizontal (Fig. 1*A*). Initially, the primary root of each newly transferred seedling was ~1 cm in length, and it grew vertically downward until encountering the physical barrier. It then grew almost exclusively on the surface of the barrier plane for 10–14 d. We used a translating stage moving perpendicular to a laser sheet to illuminate successive cross sections of the root and captured the resulting images with a digital camera (Fig. 1*A*) (24). The resulting image stack was then analyzed in MATLAB, and the 3D root morphology was reconstructed (Fig. 1*B*). Undulations of the root perpendicular to the barrier surface were generally not observed but, when they did occur, were 1 mm or less. Thus, we projected the 3D root path onto the 2D plane of the growth barrier and used this digitized trajectory in our analysis.

Results and Discussion

Coiling, Waving, and Skewing Morphologies. The morphology of *Medicago* exhibits distinct regimes as the tilt angle of the mechanical barrier θ is increased from 0° to 50°. When the plane is horizontal, the primary root meanders on the surface, with segments of alternating chirality that make incomplete planar coils before reversing their direction (Fig. 2*A*). As expected, these reversals exhibit no in-plane directional preference, which is consistent with the uniform gravitational signal across the horizontal growth plane. Owing to the random coils that dominate the morphology and similarity to growth response observed in *Arabidopsis*, this regime is referred to as "root coiling" (29, 30).

When a nonzero tilt angle is introduced to the mechanical barrier ($\theta > 0°$), the gravitational signal along the growth plane is no longer uniform, and the symmetry of the system is broken. The root now has a net growth directed downhill, a manifestation of its expected response to gravity (Fig. 2 *B* and *C*). We continue to observe root segments with alternating chirality of bending, but the length of each segment is increasingly shorter and more regular as θ increases. At a tilt of $\theta = 25°$, we observe nearly periodic reversals of root bending that resemble the sinusoidal wave reported in *Arabidopsis*, where the morphology is called "root waving" (29, 30).

As the tilt angle is further increased to $\theta = 50°$, the waving oscillations become less pronounced, and the root appears to grow in a more linear fashion along the downhill direction (Fig. 2*D*). This regime is known as "root skewing" due to the skewed growth trajectories (29, 30).

Thus far, the only experimental parameter varied is the tilt angle of the physical barrier. However, the root morphologies have changed from a random meandering root path to a regular

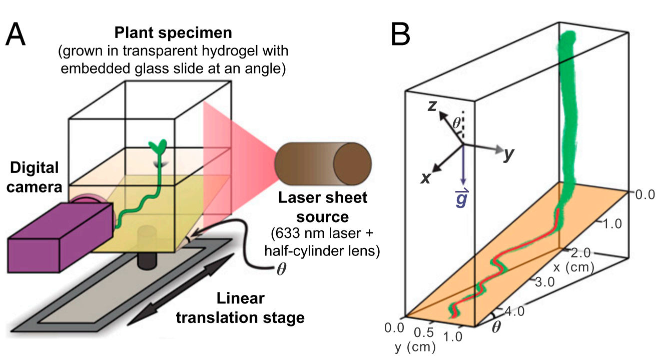

Fig. 1. Schematic of experimental setup and definition of coordinate system. (*A*) Diagram of apparatus used to scan the full 3D root morphology of *Medicago truncatula* grown in a hydrogel medium. (*B*) Example 3D reconstruction of a *Medicago* root (green) and extracted centerline used for analysis (red line). In this specific example, the inclined glass plane (orange) is at an angle $\theta = 12°$. For each angle, the *xy* coordinate system is defined on the tilted surface.

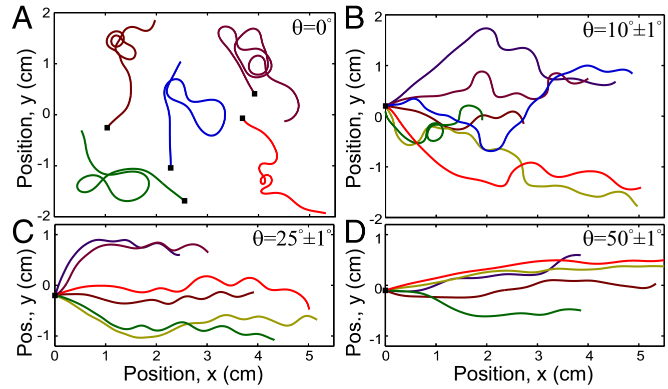

Fig. 2. Overlays of several *Medicago* root centerlines grown on planes tilted at various angles. As the tilt θ increases, the root morphologies transition from (*A*) a random, meandering root path at $\theta = 0°$ to (*B* and *C*) a sinusoidal pattern around $\theta = 10°$ (*B*) to 25° (*C*) and, ultimately, (*D*) a skewed trajectory with small undulations at $\theta = 50°$. In each panel, there are multiple root paths shown in different colors, and the point where each root makes first contact with the tilted plane is marked with a black square. For clarity, *A* has the black squares spread out, and *B*–*D* have the squares starting at $x = 0$ cm with growth generally proceeding toward the right.

sinusoidal wave and, finally, to a relatively straight skewed path. This observation suggests that the distinct morphologies have common underlying causal mechanisms and thus can be viewed in a unified fashion. To test this hypothesis, we first quantify the root morphologies and their dependence on the barrier tilt angle θ.

Curvature and Morphological Quantification. Active regulation of root morphology by biomolecular processes manifests at the tissue scale by asymmetric elongation of new growth. This differential elongation enables spatial and temporal variations in the root's curvature that can be measured experimentally, and may ultimately be useful for testing mathematical models of root development (*SI Appendix*, Fig. S1). To quantify *Medicago* root waving, we calculated the curvature κ as a function of arc length s (Fig. 3*A*). Defining the bearing angle $\psi(s)$ as the angle between the root's tangent vector $\hat{t}(s)$ and the x axis, $\kappa(s)$ is given by $d\psi(s)/ds$. Plotting the curvature as a function of arc length at consecutive times shows that as the root grows and the arc length increases, the curvature 3 mm behind the root tip maintains a constant morphology, as indicated by the vertical time-independent stripes (Fig. 3*B*, $\theta = 16°$, 110 h of growth). These time-lapse data demonstrate that the root steadily elongates at about 200 μm/h and oscillates in the elongation zone, which is the region within ~ 3 mm of the root tip (Fig. 3*B* and Movie S1). Beyond this zone, the rest of the morphology remains static, and, consequently, the root's curvature can be accurately studied by a single scan recorded after many hours of growth.

Although κ continuously varies along the root's arc length, there are well-defined regions of positive and negative curvature. These regions are bound by switching points, positions where the root changes direction (Fig. 3*A*, blue crosses where $\kappa = 0\ \mathrm{cm}^{-1}$). Noticing that the range of curvature values varies with θ (Fig. 2), we extracted the maximum curvature magnitude $|\kappa_{max}|$ from each segment between switches as a simple means to characterize the morphology (Fig. 3*C* and *SI Appendix*, Fig. S2). The resolution of our 3D imaging and reconstruction technique set a lower limit of $0.5\ \mathrm{cm}^{-1}$ on the curvature values that can be reliably measured (Fig. 3*C*, red line and shaded region indicate below-threshold measurements, and *SI Appendix*, Fig. S3). Moreover, samples that clearly demonstrate root waving show an initial period of nearly straight growth (Fig. 3*A*, $s < s_0$). To eliminate this transient growth period from our analysis, we set a curvature threshold of $1\ \mathrm{cm}^{-1}$ for all samples to define the point s_0 where root patterns begin to emerge (Fig. 3*C*, blue line). A scatter plot shows that the

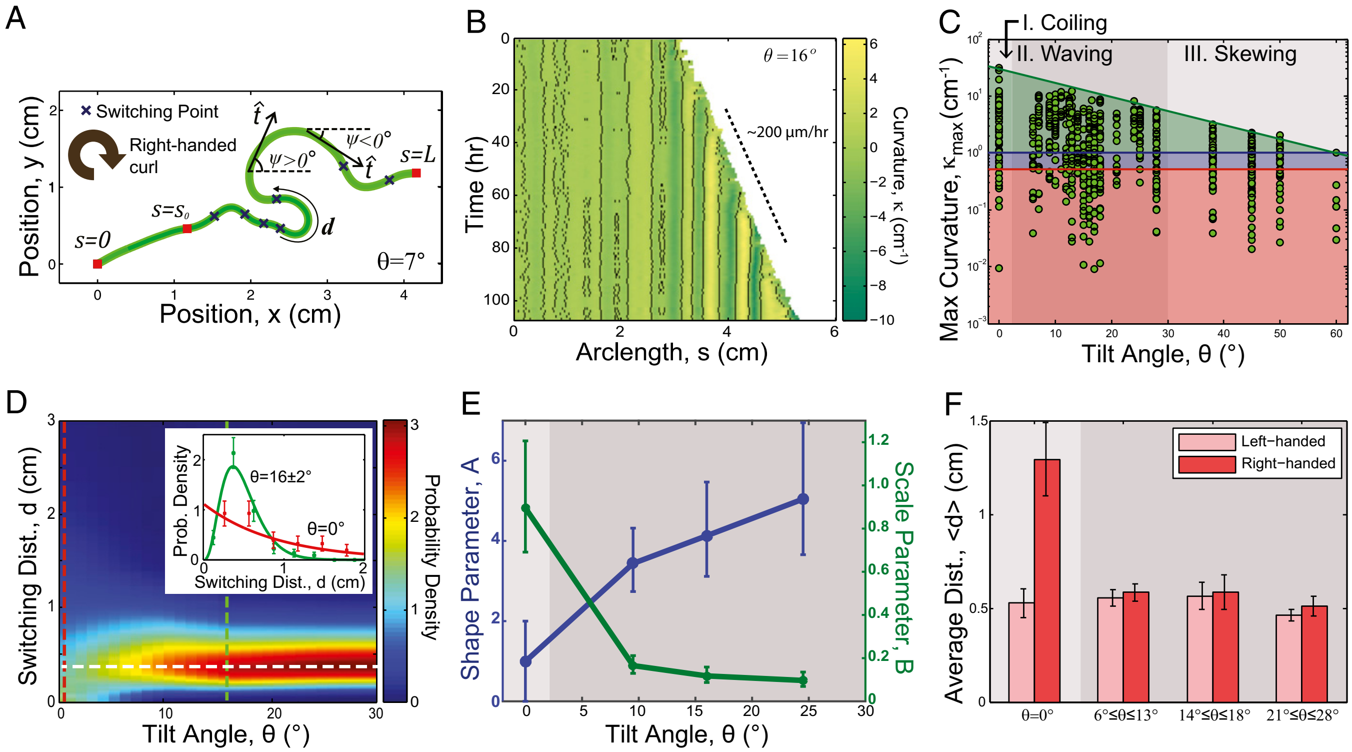

Fig. 3. Quantification of *Medicago* root growth shows smooth transitions between root morphologies. (*A*) A 2D morphology of a typical *Medicago* primary root (green line). The three red squares represent the points where the root first encounters the glass plane ($s=0$), the point where waving begins ($s=s_0$), and the root tip ($s=L$). Our analysis only includes root segments between $s=s_0$ and $s=L$, where s_0 is defined as the first switching point of the segment with curvature greater than 1 cm^{-1}. The angle between the tangent $\hat{t}$ and the horizontal $\hat{x}$ is the bearing angle, ψ. (*B*) A kymograph showing the curvature κ along the arclength s as a function of time. Black pixels indicate the reversal points measured for each time point. The color intensity denotes the magnitude of curvature in cm^{-1}. The vertical nature of the striations indicates that the curvature remains steady in time. (*C*) The spread of $|\kappa_{max}|$ from each segment of root between switching points at a given tilt angle θ. Data below the red line are below the measurement threshold and are not used in our analysis. The blue line corresponds to the initiation point s_0 where root patterns begin to emerge. The green shaded region that bounds all of the measurements has an upper limit that smoothly varies with θ, showing no obvious transitions between regions typically defined as coiling, waving, and skewing (gray bands). (*D*) An interpolated heat map representation of the switching distance probability density $P(d)$ shows an intensity peak centered on $d\approx0.4$ cm (white dashed line). Taking cuts (red, green dashed lines) and plotting the measured distributions along with fits shows comparisons with a negative exponential distribution at $\theta=0°$ (*Inset*, red), and a representative example of the gamma distribution for $\theta=(16\pm2)°$ (*Inset*, green). (*E*) The maximum likelihood estimation of the shape parameter A and scale parameter B for the probability distribution of switching distance $P(d)$. Error bar represents 95% confidence interval. $A=1$ for $\theta=0°$ as the distribution is fitted to a negative exponential distribution (*SI Appendix*, Fig. S4). Background shading is consistent with labeling in *C*. (*F*) Bias in the chirality of switching distance defined in *A*. The bar chart shows the average switching distance d of left- and right-handed segments at different θ, defined by the right-handed curl shown in Fig. 3*A*. Background shading is consistent with labeling in *C*. For *D*–*F*, each sample grouping has n between 60 and 90.

upper limit in $|\kappa_{max}|$ smoothly varies with decreasing θ, lending support to the hypothesis that different root morphologies share a common underlying mechanism (Fig. 3*C*, green line).

Distribution of Directional Switching. To further characterize *Medicago* root growth responses on tilted barriers, we measured the arc length distance d between points of zero curvature on each sample (*SI Appendix*, Fig. S4). Phenomenologically, features in the data were captured by binning over θ and fit to a probability distribution for d (Fig. 3*D*). To determine an appropriate distribution, we consider that when $\theta=0°$, the root morphology is reminiscent of a random polymer coil (32), whereas, in the waving and skewing regimes, the morphology is far more regular (Figs. 2 and 3*D*, *Inset*). A simple two-parameter function that captures this full range of switching behavior is the gamma distribution. This distribution is characterized by the shape parameter A and the scale parameter B, and is described by the density function $P(d;A,B)=e^{-d/B}d^{A-1}/B^{A}\Gamma(A)$, where $\Gamma(A)$ is the gamma function evaluated at A. Fits for $\theta=0°$ (Fig. 3*D*, *Inset*, red) and $\theta=16°$ (Fig. 3*D*, *Inset*, green) show how this function performs for two different root growth responses. Plotting an interpolated heat map of the fitted data shows a peak associated with root waving, around the cut where $d\approx0.4$ cm, that diminishes at lower tilt angles (Fig. 3*D*, dashed white line; *SI Appendix*, Fig. S4). This cut through distribution space demonstrates that transitions between root coiling (Fig. 3*D*, red dashed line) and root waving (Fig. 3*D*, green dashed line) are smooth, and suggests these morphologies arise from the same mechanical considerations, particularly because the characteristic half-oscillation length of 0.4 cm appears independent of θ. At higher tilt angles ($\theta>30°$), we find that the necessary curvature threshold for distinguishing transient growth behavior ($s<s_0$) eliminated half of the roots from consideration (*SI Appendix*, Fig. S3). Because these data may not be representative of the underlying growth response, we apply a cutoff at $\theta=30°$ to our analysis that depends on the switching distance d.

While inspecting the fitted values for A and B along with their 95% confidence intervals (Fig. 3*E* and *SI Appendix*, Fig. S4), we found that the distribution with a horizontal barrier ($\theta=0°$) has comparable fits whether we allowed A to vary ($R^2=0.85$) or fixed $A=1$ ($R^2=0.82$; see *SI Appendix*, Fig. S4). This special case with fixed A simplifies the gamma distribution to a negative exponential distribution, indicating that reversals on a flat surface can be quantitatively described by a Poisson process. This property is found when each reversal event is independent of previous reversals, or, in other words, the reversals are memoryless. Memoryless behavior, however, is lost when the tilt angle θ is nonzero. The gravitational bias introduced by the tilted mechanical barrier breaks the symmetry in the system, bringing the root from a state of random coiling to a state of more regular waving. Additionally, this symmetry-breaking barrier drives a transition from chiral to achiral morphologies, which is most clearly evident by averaging the switching distance d for each binned value of θ for left- and right-handed coils (Fig. 3*F*). We find that in the symmetric $\theta = 0°$ case, there is a clear dominance of right-handed coils, whereas nonzero values of θ have equal amounts of left- and right-handed coiling behavior. This preference for right-handed chirality in *Medicago* roots was previously seen in observations of helical root buckling, where its origin was attributed to twisted growth in the root's elongation region (24).

Interpretation of Root Morphologies by Analogy to *Escherichia coli* Chemotaxis. We have shown that the three distinct coiling, waving, and skewing morphologies of *Medicago* roots can be viewed in a unified fashion, where the different transitions are driven by changes in the growth barrier tilt angle θ. To understand the underlying mechanism, we look to bacterial foraging behaviors for a useful analogy. Specifically, *E. coli* uses chemotaxis to navigate its environment for food and nutrient resources. Broadly, the process is characterized by a series of straight-line motions punctuated by periods of random reorientation. In a chemically uniform environment, this "run-and-tumble" (33) motion exhibits the exponentially distributed run lengths indicative of a memoryless Poisson process (34). When nutrient resources are introduced and a chemical gradient is established, this unbiased random walk becomes asymmetric; runs along the direction of steepest gradient have a longer duration than runs in the transverse direction. Thus, despite the randomizing effect of tumbles, *E. coli* is able to swim in a favorable direction (Fig. 4).

By inspecting the reversals of *Medicago* root trajectories, we see a behavior analogous to *E. coli*'s run-and-tumble motion. In essence, the tilted mechanical barrier establishes a gravitational gradient akin to the chemical gradient in *E. coli* chemotaxis. When the mechanical barrier is horizontal ($\theta = 0°$), the root performs a random walk, in the sense that the switching distance d is exponentially distributed and the reversal events are a Poisson process (Fig. 3*D*, *Inset*). Because the root experiences uniform gravitational stimulus, it grows without any directional preference (Figs. 2*A* and 4). However, when the mechanical barrier is tilted ($\theta > 0°$), the root is able to move through the gravitational gradient, yielding trajectories biased toward the downhill direction (Fig. 2 *B* and *C*). With increasing θ, the root becomes increasingly more biased, so that at $\theta = 50°$, the root hardly deviates from the x axis (Fig. 2*D*). Hence, the unifying mechanism behind root coiling, waving, and skewing can be considered a form of root "grow-and-switch" gravitropism (Fig. 4). In this picture, *Medicago*'s root growth is like *E. coli*'s runs, whereas *Medicago*'s switching points are like *E. coli*'s tumbles. We therefore predict that just as *E. coli*'s rate of "run-and-tumbling" is dependent on the strength of the chemical gradient, *Medicago*'s rate of directional reversal will depend on the strength of the gravity gradient.

To test this prediction of the grow-and-switch gravitropic interpretation, we discretize the root into small segments of length 0.04 cm and compute the probability that a segment at a particular bearing ψ occurs at a reversal point. Although this probability is equal to the rate of reversal, each reversal event itself can be identified as either correct or incorrect depending on whether the subsequent root trajectory aligns toward either the downhill or transverse direction (Fig. 5*A*). Thus, by analogy to chemotaxis, we expect that the further the root deviates from $\psi = 0°$, the more likely it is to make a correct reversal. Plotting the measured rate of correct reversals against ψ for $6° \le \theta \le 13°$ shows that *Medicago* follows this expected behavior (Fig. 5*B*, red data and linear fits). Indeed, data for θ throughout the root waving regime exhibit such dependencies (Fig. 5*B*, green and blue data), and exhibit a V-like shape centered at $\psi = 0°$ with the slope becoming larger as the tilt θ increases. These trends demonstrate that gravitropism is biasing the statistical properties

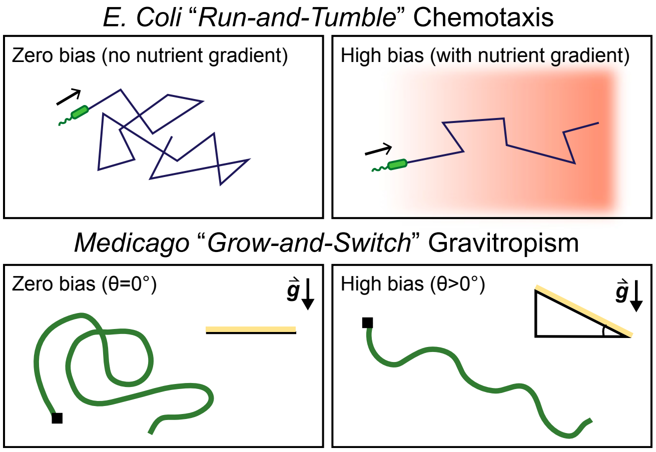

Fig. 4. A comparison between *E. coli* run-and-tumble chemotaxis and *Medicago* grow-and-switch gravitropism. When moving within an environment of uniform chemical gradient, *E. coli* executes a random walk. However, this random walk is biased when a nutrient gradient is established and the net displacement of *E. coli* is in the direction of high nutrient concentration. Similarly, the root path of *Medicago* growing on a horizontal plane ($\theta = 0°$) is random and has no directional preference. When a gravitational bias is introduced by tilting the growth plane such that $\theta > 0°$, the root path has a net direction downhill driven by the gravitropic tendencies of root growth.

of the reversal events. In this analysis, we excluded outlier reversals occurring at extreme values of ψ by requiring at least two counts in each binned value for ψ (see *SI Appendix*, Fig. S5 for full histogram data). When $\theta = 0°$, the choice of $\psi = 0°$ is arbitrary and reversal events are neither correct nor incorrect, because there is no gravitational gradient. Plotting the rate of all reversals for $\theta = 0°$ (Fig. 5*B*, black data and linear fit) shows no directional preference in the bearing angle ψ, consistent with expectations based on *E. coli*'s behavior in a chemically isotropic environment. Thus, the plots of reversal rate for varying θ further support the analogy between *Medicago* grow-and-switch gravitropism and *E. coli* run-and-tumble chemotaxis.

We emphasize that for $\theta > 0°$, $(87 \pm 5)\%$ of all reversals are correct reversals. This imbalance implies that in addition to sensing its bearing with respect to gravity, the root also has information about the sign of the root path curvature. Otherwise, reversal events would only be in the correct direction half of the time. Because curvature is determined by derivatives of the root's trajectory, the root must have information that extends over some physical distance. Whether this distance is a few cells or a few centimeters remains unclear; however, the preference for correct reversals indicates that the underlying mechanism for root waving involves nonlocal information.

The data show that the range of observed bearing angle ψ decreases with increasing tilt θ (Fig. 5*B*). This reduced range suggests the presence of a θ-dependent threshold, beyond which the root will reverse its direction to navigate downhill. Because the root can only measure its orientation with respect to gravity (35–39), we use a trigonometric analysis to define the the angle ϕ between the root tip tangent and the gravity vector by $\phi = \arccos[\cos(\psi)\sin(\theta)]$. Plotting the root's angle with respect to gravity ϕ versus the bearing angle ψ shows that there is a well-defined minimum value at $\psi = 0°$ (Fig. 5*C*, *Inset*, minimum of purple, blue, red, and green curves). As the barrier's tilt angle is varied, however, there is a range of maximum angles the root tip makes with respect to gravity, ϕ_{max} (Fig. 5*C*, *Inset*, limits of colored lines). A scatter plot of ϕ_{max} for all tilt angles $\theta > 0°$ shows a linear trend (Fig. 5*C*, blue data and line; $R^2 = 0.81$) that parallels the line of minimum ϕ (Fig. 5*C*, lower dashed line). These data include roots grown on barriers with $\theta > 30°$ because the measurements of ϕ_{max} are insensitive to the threshold process applied to the switching distance d. Remarkably, the range

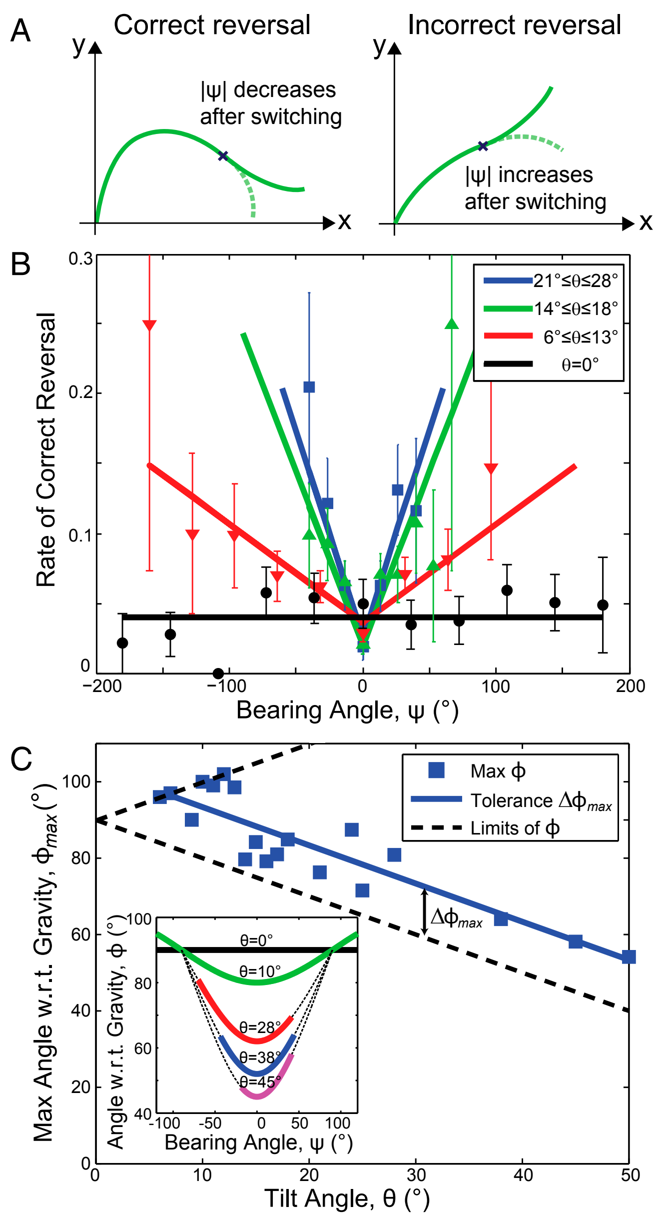

Fig. 5. Extracting the principles of *Medicago* grow-and-switch gravitropism. (*A*) Illustrations of correct and incorrect reversals. A correct reversal immediately decreases the bearing ψ so that the root is more aligned with the downhill direction. An incorrect reversal sends the root in a transverse direction. (*B*) The rate of correct reversals plotted against bearing angle ψ shows that when the tilt angle θ increases, the root is able to find the downward direction more efficiently. In the special case where $\theta = 0°$, there is no distinction between correct and incorrect reversals, and we therefore include all reversal events in the plot (black data and line). (*C*) Given a specific tilt angle θ, there are physical limits to the angle with respect to gravity ϕ (black dashed lines). Plotting the maximum angle with respect to gravity $\phi_{\max}$ for each value of θ gives a scatter plot that shows a characteristic range of values that is $\Delta\phi_{\max}$ greater then the physical limit. This angle $\Delta\phi_{\max}$ can be considered *Medicago*'s tolerance for sensing the direction of steepest descent. *Inset* shows the angle with respect to gravity ϕ plotted against the bearing angle ψ for a few representative values of tilt angle θ. The dashed lines are calculated from a trigonometric analysis, and the upper limit for each colored line is used in the scatter plot of *C*.

of ϕ between its minimum and maximum values, $\Delta\phi_{\max}$, for different tilts is nearly constant (Fig. 5*C*), indicating that grow-and-switch gravitropism has a characteristic angle range, with respect to gravity, of $\sim(14 \pm 6)°$ (mean ± SD), at which point the root switches direction to move more directly downhill. This characteristic angle can therefore be construed as the measurement tolerance of *Medicago*'s gravity sensing abilities.

In our quantification of *Medicago*'s root growth, we found several indications of smooth transitions between different morphologies. For example, the upper bound on the maximum curvature $\kappa_{\max}$ smoothly varied with tilt θ and had no obvious transitions between root coiling and root waving or root waving and root skewing (Fig. 3*C*). Similarly, the switching distance d exhibited smooth behavior between root coiling and root waving (Fig. 3*D*), which is also evident in the gamma distribution fitting parameters A and B (Fig. 3*E*). This finding is consistent with our analysis of the reversal rates, where the wedge-shape trend in bearing angle ψ visibly narrows with increasing barrier tilt θ (Fig. 5*B*). Although the resolution of curvature measurements does not permit us to distinguish whether root skewing consists of low-amplitude root waving, we also note that the maximum angle with respect to gravity $\phi_{\max}$ smoothly decreases across all three morphologies (Fig. 5*C*). Taken as a whole, these data reinforce the overall interpretation that divisions between phenotypes can be unified by the grow-and-switch mechanism proposed here.

Conclusion

Inspired by *E. coli*'s run-and-tumble approach to chemotaxis, our experiments and analysis indicate that *Medicago*'s coiling and root waving growth response arise from a grow-and-switch gravitropism. Whereas previous studies with *Arabidopsis* (25–30) have examined genetic and temporal properties of root waving, the interpretation proposed here is based on the observation of continuous transitions between root morphologies, as well as a statistical analysis of the root's directional switching. The data show that switching events are related to the root's growth direction with respect to gravity, and are governed by the root's ability to measure the direction of gravity within some precision, which roughly corresponds to $\Delta\phi_{\max}$. Thus, just as bacterial chemotaxis is enabled by *E. coli*'s ability to measure a differential nutrient concentration along straight runs, *Medicago*'s ability to find the path of steepest descent is enabled by the root's capacity to sense orientation relative to gravity. Because this growth strategy aids in navigating highly obstructed environments, we speculate that grow-and-switch gravitropism may have been an evolutionarily favorable trait for *Medicago*.

By casting root morphologies in a framework similar to *E. coli* chemotaxis, we offer a simplified model for phenotype regulation that can be further studied at genetic and biomolecular levels. The analogy to *E. coli*, however, was not unique, as a number of other cells, including amoeba, *Dictyostelium discoideum*, and mammalian neutrophils, show chemotactic behavior (40). In particular, *Dictyostelium* is known to execute directed drifts along nutrient gradients (41–43). This behavior is mediated by transient pseudopod formation fronts that drive changes in the direction of motion. Although there are multiple organisms that use this type of "try-and-correct" strategy, the microscopic origin for how directional switching is executed in *Medicago* remains to be discovered. One possibility is a time-delayed gravitropic signal measured by statoliths in the root tip (35–39) that propagate back to the elongation region. This proposal is consistent with time-lapse data (Fig. 3*B* and Movie S1) showing transient curvature reversal events, which may be related to the asymmetry between correct and incorrect reversals. Alternatively, differential elongation coupled to a touch-activated twisting mechanism previously reported in *Medicago* (24) may also generate the necessary switching. In either case, these hypothesized mechanisms may be distinguished by their ability to understand and predict the characteristic root waving length of ~0.4 cm. Ultimately, a set of detailed and in-depth experiments combining mechanical and biological approaches are required to further probe the origins of *Medicago*'s directional switching.

A benefit of the analogy between *Medicago* and *E. coli* proposed here is that studies already conducted in the context of bacterial chemotaxis can inspire new studies in root growth. For example, experiments that involve dynamically changing chemical gradients have helped probe the biochemical origins of chemotaxis. Inspired by such studies, we conceptually map these dynamic chemical gradients to dynamic gravity gradients, and consider the potential opportunities of a variably tilting barrier. This modification could be accomplished either with a barrier that has sections with different tilted angles or by attaching the sample box to a rotating stepper motor. In either case, one could explore the timescale for how long it takes roots to respond to changes in gravity gradients. Alternatively, taking inspiration from studies that examine bacterial quorum sensing, we could probe the analogous scenario of root–root interactions between same-species plants or species that are known to compete for resources (44). It would also be interesting to probe how roots respond to multiple conflicting tropisms by incorporating a nutrient gradient along a different direction than the gravity gradient. Such future studies aside, we expect that these efforts to better understand interactions between mechanical and biological regulation should enhance our understanding of root system architectures and the strategies plants use to navigate their environment.

ACKNOWLEDGMENTS. We dedicate this work in memory of Chris Henley, whose tireless efforts have helped make this work possible. The authors thank A. Geitmann for insightful conversations. We also thank S. Gerbode and S. Imes for apparatus development. T.H.T. was supported by Cornell's Engineering Learning Initiative. J.L.S. was supported by the National Science Foundation through a Graduate Research Fellowship. Research in the M.J.H. lab was supported by the National Science Foundation through Grants IOS-1127155 and IOS-1353367. C.L.H was supported by the US Department of Energy through Grant DE-FG02-89ER-45405. I.C. was supported by a National Science Foundation Grant DMR-1056662.

1. Esmon CA, Pedmale UV, Liscum E (2005) Plant tropisms: Providing the power of movement to a sessile organism. *Int J Dev Biol* 49(5-6):665–674.
2. Hopkins WG, Hüner NPA (1995) *Introduction to Plant Physiology* (Wiley, New York), Vol 355.
3. Hart JW (1990) *Plant Tropisms: And Other Growth Movements* (Springer, New York).
4. Firn RD, Digby J (1980) The establishment of tropic curvatures in plants. *Annu Rev Plant Physiol* 31(1):131–148.
5. Schrank AR (1950) Plant tropisms. *Annu Rev Plant Physiol* 1:59–74.
6. Armon S, Efrati E, Kupferman R, Sharon E (2011) Geometry and mechanics in the opening of chiral seed pods. *Science* 333(6050):1726–1730.
7. Gerbode SJ, Puzey JR, McCormick AG, Mahadevan L (2012) How the cucumber tendril coils and overwinds. *Science* 337(6098):1087–1091.
8. Stuhlman O (1948) A physical analysis of the opening and closing movements of the lobes of venus' fly-trap. *Bull Torrey Bot Club* 75(1):22–44.
9. Williams SE, Bennett AB (1982) Leaf closure in the venus flytrap: An acid growth response. *Science* 218(4577):1120–1122.
10. Hodick D, Sievers A (1989) On the mechanism of trap closure of Venus flytrap (*Dionaea muscipula* Ellis). *Planta* 179(1):32–42.
11. Forterre Y, Skotheim JM, Dumais J, Mahadevan L (2005) How the Venus flytrap snaps. *Nature* 433(7024):421–425.
12. Thitamadee S, Tuchihara K, Hashimoto T (2002) Microtubule basis for left-handed helical growth in *Arabidopsis*. *Nature* 417(6885):193–196.
13. Ishida T, Kaneko Y, Iwano M, Hashimoto T (2007) Helical microtubule arrays in a collection of twisting tubulin mutants of *Arabidopsis thaliana*. *Proc Natl Acad Sci USA* 104(20):8544–8549.
14. Barley KP, Farrell DA, Greacen EL (1965) The influence of soil strength on the penetration of a loam by plant roots. *Soil Res* 3(1):69–79.
15. Dexter AR (1987) Mechanics of root growth. *Plant Soil* 98(3):303–312.
16. Bengough AG, Mullins CE (1990) Mechanical impedance to root growth: A review of experimental techniques and root growth responses. *J Soil Sci* 41(3):341–358.
17. Bengough AG, Croser C, Pritchard J (1997) A biophysical analysis of root growth under mechanical stress. *Plant Roots—From Cells to Systems*, eds Anderson HM, Barlow PW, Clarkson DT, Jackson M, Shewry PR (Springer, New York), pp 107–116.
18. Clark LJ, Whalley WR, Barraclough PB (2003) How do roots penetrate strong soil? *Roots: The Dynamic Interface Between Plants and the Earth*, ed Abe JJ (Springer, New York), pp 93–104.
19. Bengough AG, McKenzie BM, Hallett PD, Valentine TA (2011) Root elongation, water stress, and mechanical impedance: A review of limiting stresses and beneficial root tip traits. *J Exp Bot* 62(1):59–68.
20. Abdalla AM, Hettiaratchi DRP, Reece AR (1969) The mechanics of root growth in granular media. *J Agric Eng Res* 14(3):236–248.
21. Whiteley GM, Dexter AR (1984) The behaviour of roots encountering cracks in soil. *Plant Soil* 77(2-3):141–149.
22. Dexter AR, Hewitt JS (1978) The deflection of plant roots. *J Agric Eng Res* 23(1):17–22.
23. Whiteley GM, Hewitt JS, Dexter AR (1982) The buckling of plant roots. *Physiol Plant* 54(3):333–342.
24. Silverberg JL, et al. (2012) 3D imaging and mechanical modeling of helical buckling in *Medicago truncatula* plant roots. *Proc Natl Acad Sci USA* 109(42):16794–16799.
25. Okada K, Shimura Y (1990) Reversible root tip rotation in *Arabidopsis* seedlings induced by obstacle-touching stimulus. *Science* 250(4978):274–276.
26. Simmons C, Söll D, Migliaccio F (1995) Circumnutation and gravitropism cause root waving in arabidopsis thaliana. *J Exp Bot* 46(1):143–150.
27. Migliaccio F, Piconese S (2001) Spiralizations and tropisms in *Arabidopsis* roots. *Trends Plant Sci* 6(12):561–565.
28. Thompson MV, Holbrook NM (2004) Root-gel interactions and the root waving behavior of Arabidopsis. *Plant Physiol* 135(3):1822–1837.
29. Oliva M, Dunand C (2007) Waving and skewing: How gravity and the surface of growth media affect root development in *Arabidopsis*. *New Phytol* 176(1):37–43.
30. Migliaccio F, Fortunati A, Tassone P (2009) *Arabidopsis* root growth movements and their symmetry: Progress and problems arising from recent work. *Plant Signal Behav* 4(3):183–190.
31. Floss DS, et al. (2013) Gene silencing in *Medicago truncatula* roots using RNAi. *Methods Mol Biol* 1069:163–177.
32. Sperling LH (2005) *Introduction to Physical Polymer Science* (Wiley, New York).
33. Berg HC, Brown DA (1972) Chemotaxis in *Escherichia coli* analysed by three-dimensional tracking. *Nature* 239(5374):500–504.
34. Berg HC (2004) *E. coli in Motion* (Springer, New York).
35. Moulia B, Fournier M (2009) The power and control of gravitropic movements in plants: A biomechanical and systems biology view. *J Exp Bot* 60(2):461–486.
36. Baldwin KL, Strohm AK, Masson PH (2013) Gravity sensing and signal transduction in vascular plant primary roots. *Am J Bot* 100(1):126–142.
37. Leitz G, Kang B-H, Schoenwaelder MEA, Staehelin LA (2009) Statolith sedimentation kinetics and force transduction to the cortical endoplasmic reticulum in gravity-sensing *Arabidopsis* columella cells. *The Plant Cell Online* 21(3):843–860.
38. Morita MT (2010) Directional gravity sensing in gravitropism. *Annu Rev Plant Biol* 61: 705–720.
39. Yoder TL, Zheng HQ, Todd P, Staehelin LA (2001) Amyloplast sedimentation dynamics in maize columella cells support a new model for the gravity-sensing apparatus of roots. *Plant Physiol* 125(2):1045–1060.
40. Bagorda A, Parent CA (2008) Eukaryotic chemotaxis at a glance. *J Cell Sci* 121(Pt 16): 2621–2624.
41. Gerisch G (1982) Chemotaxis in *Dictyostelium*. *Annu Rev Physiol* 44(1):535–552.
42. Amselem G, Theves M, Bae A, Bodenschatz E, Beta C (2012) A stochastic description of *Dictyostelium* chemotaxis. *PLoS One* 7(5):e37213.
43. Graziano BR, Weiner OD (2014) Self-organization of protrusions and polarity during eukaryotic chemotaxis. *Curr Opin Cell Biol* 30:60–67.
44. Paya AM, Silverberg JL, Padgett J, Bauerle TL (2015) X-ray computed tomography uncovers root–root interactions: Quantifying spatial relationships between interacting root systems in three dimensions. *Front Plant Sci* 6, 10.3389/fpls.2015.00274.

Supporting Information

Tan et al. 10.1073/pnas.1509942112

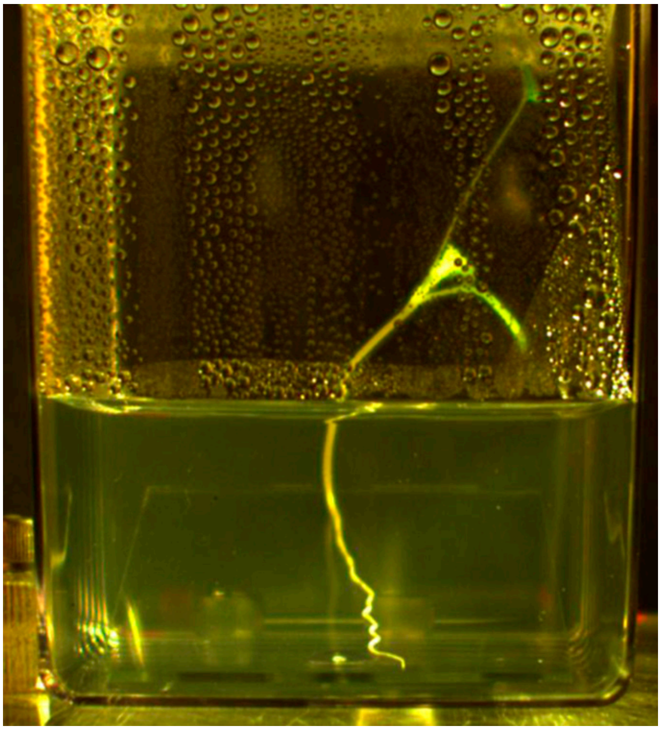

Movie S1. Time-lapse movie of a *Medicago* root growing on inclined plane $\theta = 16°$ over a period of 110 h. The transient region near the root tip is dynamic, sweeping across a range of bearing before becoming fixed.

Movie S1

Other Supporting Information Files

SI Appendix (PDF)

Supporting Information

SI Materials and Methods

Medicago sterilization and germination.

Unbroken wild type A17 *Medicago truncatula* seeds are collected and scarified by immersing them in concentrated sulphuric acid H_2SO_4 for 10 min. To ensure that the samples are sterile, the scarified seeds are soaked in 10% bleach solution (10% bleach in 0.1% Tween 20; the bleach contains 6% sodium hypochlorite) with gentle agitation in laminar flow for 10 min. For imbibition, the seeds are first placed in sterile distilled water and left on a shaker for 3 hours. Subsequently, the seeds are incubated at 4°C for 26 hours. Finally, the seeds are transferred to a petri dish and incubated at 28°C for 18 hours. Petri dishes are inverted to encourage growth of straight radicles before transplanting into a transparent growth chamber. These imbibition and incubation steps are done in unlit conditions. Between all steps, sterile distilled water is used to decant the seeds. This protocol is performed to ensure synchronized germination (see reference [31] of main text for further information).

Fahraeus media and Gelzan preparation.

Root growth experiments were carried out with *Medicago* plants grown in a Fahraeus media (F-media) hydrogel. The F-media consisted of: 0.9 mM $CaCl_2$; 0.5 mM $MgSO_4$; 20 μM KH_2PO_4; 10 μM Na_2HPO_4; 20 μM ferric citrate; 1.0 mM NH_4NO_3; 33 μg/L $MnCl_2$; 33 μg/L $CuSO_4$; 7 μg/L $ZnSO_4$*$7H_2O$; 100 μg/L H_3BO_3; 33 μg/L Na_2MoO_4; 218 mg/L MES free acid monohydrate; and 2.5 g/L Gelrite (Sigma-Aldrich) dissolved in distilled water. The gel solution was autoclaved before solidifying to ensure sterile conditions (see reference [31] of main text for further information). To create a mechanical barrier, a glass slide of appropriate length was inserted into a Magenta box (Magenta Corp.). The liquid F-media was then poured into this transparent growth container and left to solidify so that the glass slide was embedded in the hydrogel with a fixed tilt. *Medicago* seedlings were germinated until root growth was approximately 1 cm. They were then transplanted into the container allowing unobstructed vertically aligned growth until the root made contact with the glass slide. The *Medicago* plant was left to grow at room temperature with 12 hours of light per day. The roots were imaged once they reached a length of about 5-6 cm.

3D imaging setup and root reconstruction.

To acquire data for roots growing on inclined barriers where $\theta > 0°$, we used a 3D imaging system consisting of a fixed laser sheet and a translational stage enclosed in a light-controlled environment [24] (Fig. 1A of main text). Prior to imaging, the growth light is first turned off. The plant specimen, which is now under dark conditions, is translated along a linear axis through the laser sheet. While the plant moves through the plane of illumination, a digital camera acquires a series of images corresponding to each illuminated plane. This image stack is then saved for later analysis and 3D reconstruction with a voxel size of $0.1 \times 0.1 \times 0.2$ mm^3. Once image acquisition is completed, the stage resets to its initial position, and the growth light is returned to its prior state. Using MATLAB's morphological reconstruction toolbox, we are able to extract the centerline of the primary root from the raw image data with a spatial resolution of 0.3 mm (Fig. 2 of main text). For roots growing on a horizontal surface where $\theta = 0°$, we acquire image data by taking two dimensional (2D) photographs from beneath the transparent growth container. We then apply a thresholding filter to extract the centerline with a spatial resolution of 0.15 mm.

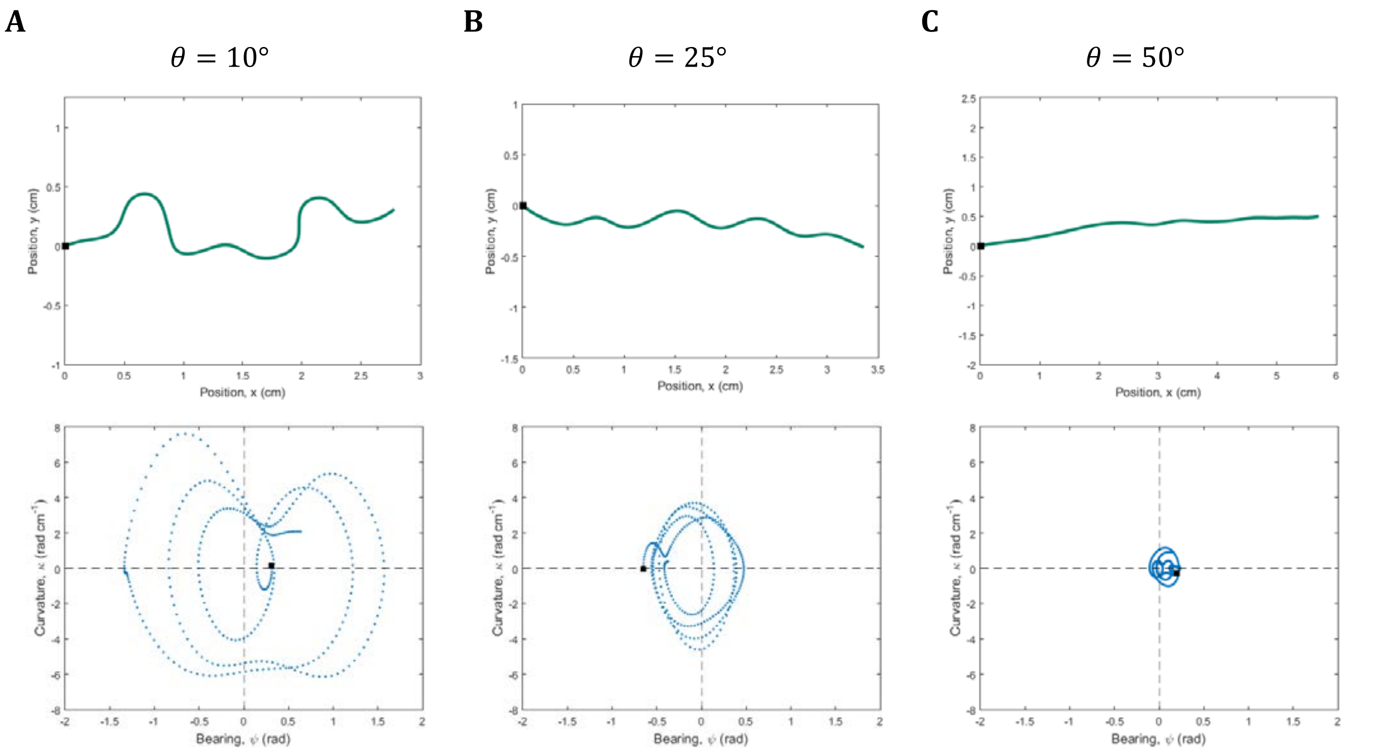

Fig. S1. Possible mathematical modeling using phase diagrams of root trajectories.

Phase diagrams of root trajectories provide a potential mathematical framework to quantitatively understand root behavior. By plotting $\frac{d\psi}{ds}$ versus $\psi(s)$ for 3 roots at $\theta = 10°$, $25°$ and $50°$ (A-C), we can follow the evolution of root curvature in phase space. The black square denotes the starting position of the root. To first order approximation, we observed that the phase trajectories eventually settle into a limiting ellipse. Therefore, we posit that the root trajectory follows the following ordinary differential equation:

$$C_1 \left(\frac{d\psi}{ds}\right)^2 + (\psi - \psi_0)^2 = C_2,$$

where ψ denotes the bearing, $\frac{d\psi}{ds}$ denotes the rate of change of bearing, and C_1, C_2, ψ_0 are parameters to be fitted. Geometrically, C_1 and C_2 characterize the wavelength and amplitude of root waving while ψ_0 characterizes the skewing angle. This approach removes the randomness in the switching mechanism, but is capable of quantifying the trend observed in root curvature at different tilt angle θ.

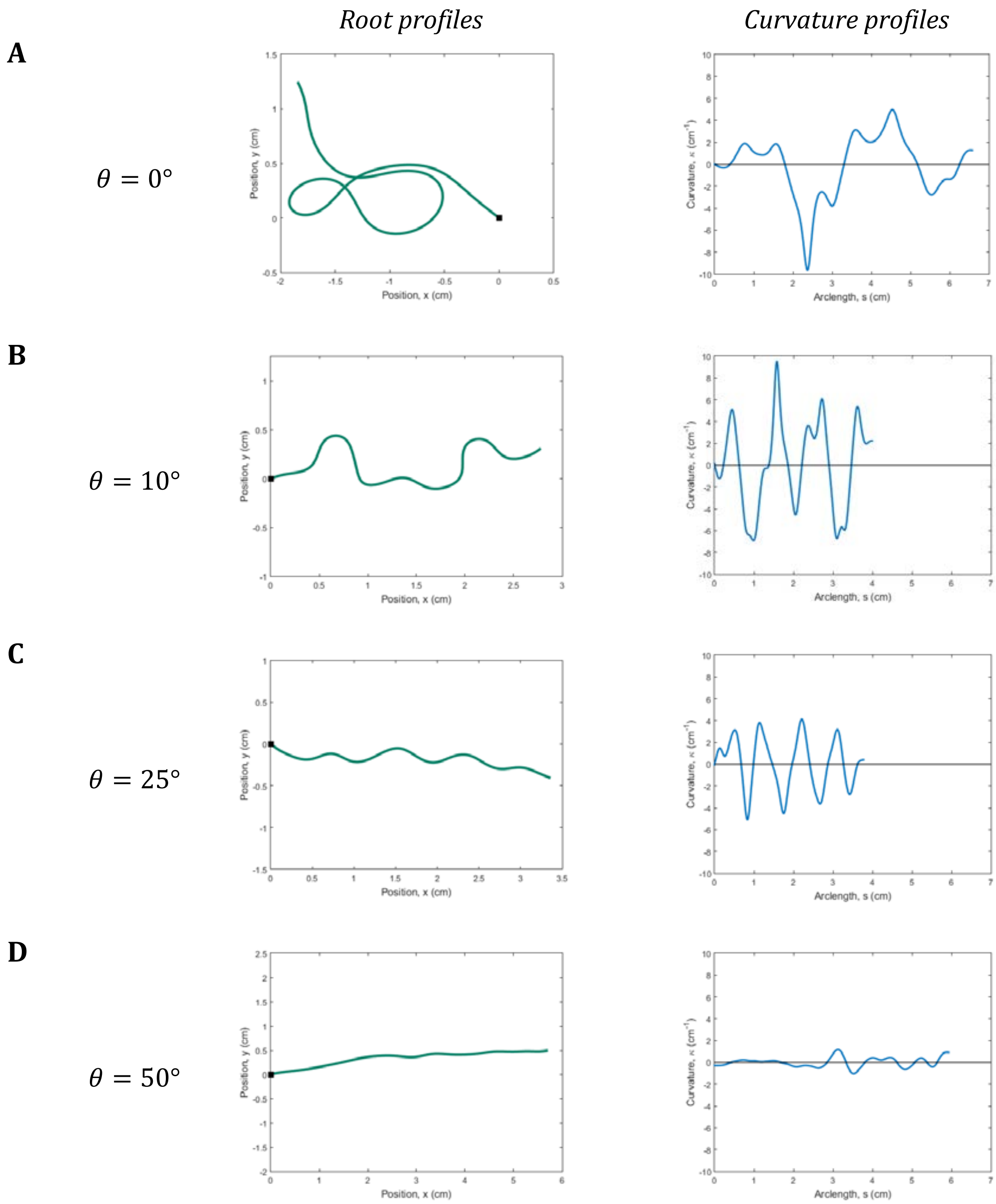

Fig. S2. curvature profiles $\kappa(s)$ **of representative root samples.**

Curvature profiles of four representative root samples. The curvature profiles of roots at different θ's (*A*-*D*) are plotted as a function of arclength s. The point where each root makes first contact with the tilted plane is marked with a black square.

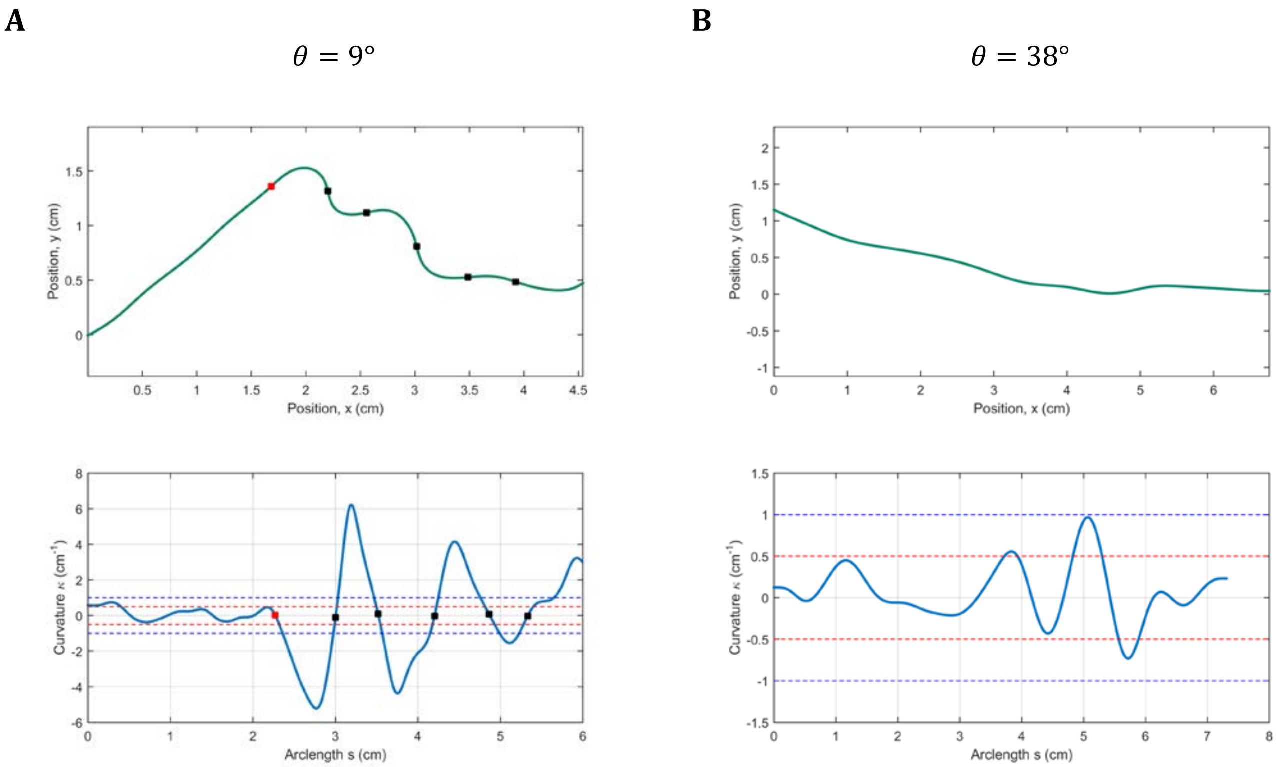

Fig. S3. Curvature resolution limit and threshold for defining *s_0*.

The resolution of our 3D imaging and reconstruction technique set a lower limit of 0.5 cm^{-1} on the curvature values that can be reliably measured (red dotted line, *A, B*). Moreover, samples that clearly demonstrate root waving show an initial period of nearly straight growth (Fig. 3A of main text, $s < s_0$). In order to eliminate this transient growth period from our analysis, we set a threshold of 1 cm^{-1} (blue dotted line, *A, B*) for all samples to define the point s_0 where root patterns begin to emerge. In the waving regime, as illustrated by a representative root at $\theta = 9°$ in (*A*), the first segment of root with curvature magnitude greater 1 cm^{-1} determines the onset of root waving (red square). In addition, we can reliably determine the switching points (black squares) because root segments have curvature magnitudes significantly greater than the resolution. However, in the skewing regime, as illustrated by a representative root at $\theta = 38°$ in (*B*), most segments have curvature values below that of our resolution and hence the switching points cannot be reliably determined. Of the 57 roots in the waving regime ($6° \leq \theta \leq 28°$), 9 roots are omitted from analyses that are dependent on reversal events because the root waving onset point s_0 cannot be determined. In the skewing regime ($30° < \theta$), 11 out of 22 roots do not have s_0 that can be reliably identified. Therefore, analyses that are dependent on reversal events are not performed on this group of roots. All roots in the coiling regime have an s_0 that can be readily determined.

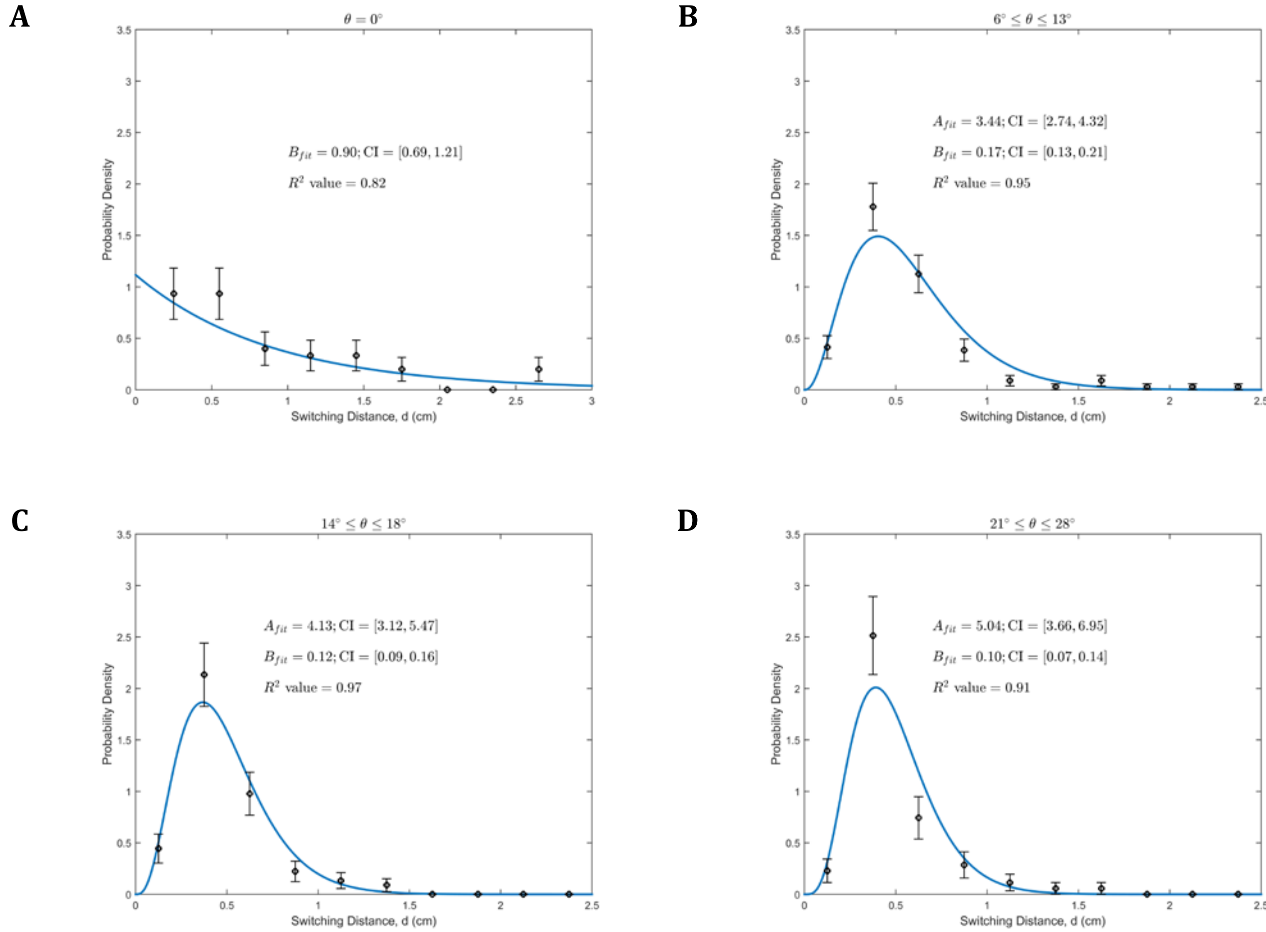

Fig. S4. Probability density of switching distance $P(d)$ using maximum likelihood estimation (MLE).

Probability distribution of switching distance $P(d)$ as a function of tilt angle θ fit to a gamma distribution (*A*-*D*). The gamma distribution is given by $P(d;A,B) = e^{-d/B}d^{A-1}/B^{A}\Gamma(A)$, where A is the shape parameter, and B is the scale parameter. The maximum likelihood estimation (MLE) of the parameters are stipulated in the respective plots. The 95% confidence interval for each parameter and the R^2 values are indicated as well. For the case of $\theta = 0$, we set $A = 1$ to simplify the gamma distribution to a Poisson distribution (negative exponential), which is known to arise in unbiased random walks.

In our analysis of the root switching distance data, we tested the log-normal and gamma distributions. While both had comparable fits with $R^2 > 0.9$ on tilted barriers, we find the gamma distribution offers a more insightful explanation of root coiling as a memoryless random process on horizontal barriers. Moreover, previous studies (see reference [33] and [34] of main text) studying *E. coli* motion in chemically uniform environments found a statistical distribution of run lengths well described by a Poisson distribution (i.e., gamma distribution with $A = 1$), which is analogous to the case of root growth on a horizontal barrier where we fit for the same function. Taken together, the insights and enhanced explanatory power of the gamma distribution motivate the analysis presented in the main text.

A $6° \leq \theta \leq 13°$

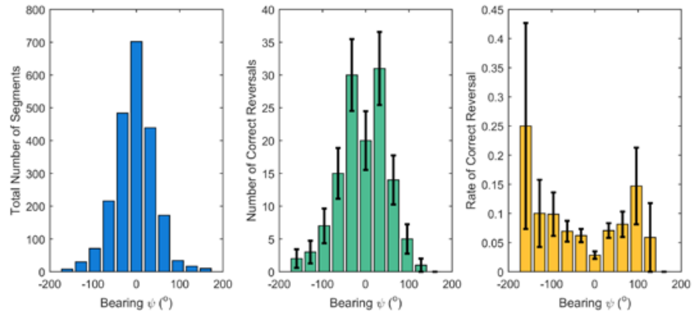

B $14° \leq \theta \leq 18°$

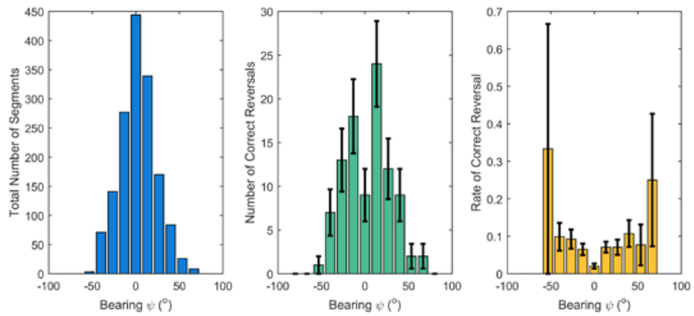

C $21° \leq \theta \leq 28°$

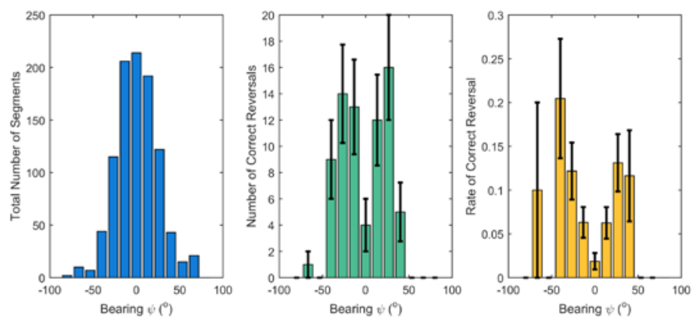

Fig. S5. Histogram of correct and incorrect reversals.

The rate of correct reversal is defined as the probability that an infinitesimal segment of root at a particular bearing ψ will reverse its chirality so that the subsequent root segments will bend in a more downhill direction (i.e. decreasing $|\psi|$, Fig. 5A of main text). To compute this reversal rate, we discretized the root into short segments of 0.04 cm long and binned them (blue, *A*-*C*). We then calculated the number of root segments within each bin that corresponded to correct reversal events (green, *A*-*C*). Dividing the number of correct reversals by the total number of segments, we obtained the rate of correct reversal (yellow, *A*-*C*). Due to “grow-and-switch” gravitropism, the rate of reversal graphs in the waving regime exhibit increasingly steeper ‘V’ shape curves as θ gets larger.

D $\theta = 0°$

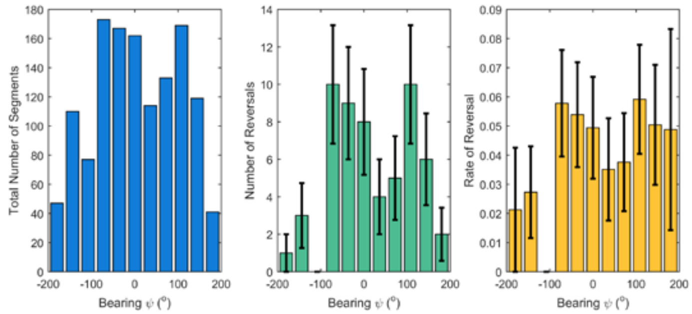

Fig. S5. Histogram of correct and incorrect reversals (continued).

Note that at $\theta = 0°$, the choice of $\psi = 0°$ is arbitrary and reversal events are neither correct nor incorrect, since there is no gravitational gradient. A similar analysis is performed to the data and the rate of reversal shows uniform distribution (*D*), consistent with expectations based on *E. coli* 's behavior in a chemically isotropic environment. To exclude outlier reversals, we do not include any data point with n=1 for analysis in Fig. 5B of main text.

E $6° \leq \theta \leq 13°$

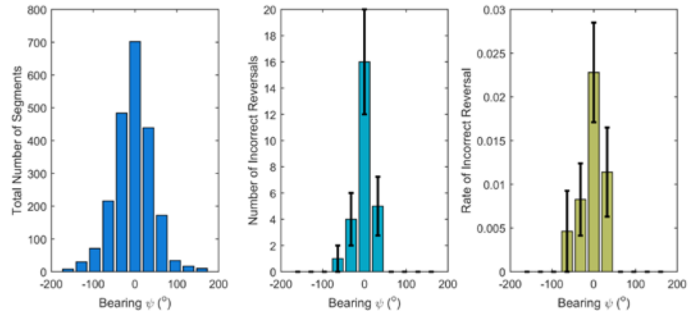

F $14° \leq \theta \leq 18°$

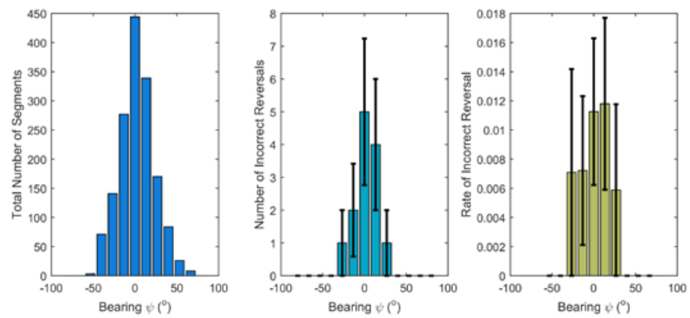

G $21° \leq \theta \leq 28°$

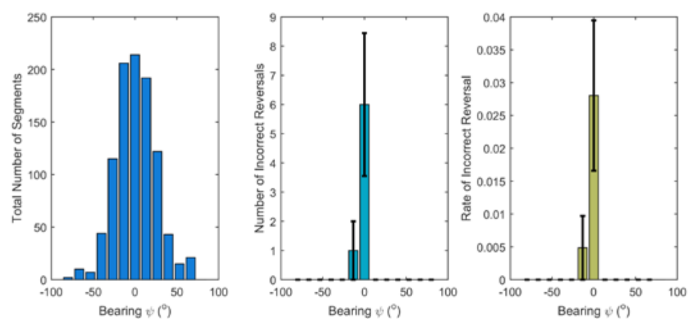

Fig. S5. Histogram of correct and incorrect reversals (continued).

Analogous to *(A-C).*, the rate of incorrect reversal is defined as the probability that an infinitesimal segment of root at a particular bearing ψ will reverse its chirality so that the subsequent root segments will bend in a less downhill direction (i.e. increasing $|\psi|$, Fig. 5A of main text). To compute this reversal rate, we discretized the root into short segments of 0.04 cm long and binned them (blue, *E-G*). We then calculated the number of root segments within each bin that corresponded to an incorrect reversal event (cyan, *E-G*). Dividing the number of incorrect reversal event by the total number of segments, we obtained the rate of wrong reversal (dark yellow, *E-G*). We observe that the incorrect reversal rate is centered at $\psi = 0°$ and the distribution gets narrower with increasing θ. This is consistent with the notion that the root is better able to find the downhill direction at large θ with less incorrect reversal.